Biomaterials Science

ROYAL SOCIETY OF CHEMISTRY

PAPER

View Article Online
View Journal | View Issue

Cite this: *Biomater. Sci.*, 2023, **11**, 6524

Biodegradable covalent organic frameworks achieving tumor micro-environment responsive drug release and antitumor treatment†

Tong Li,[a,b,d] Dianwei Wang,[a,b,d] Zhaopei Guo,[a,d] Lin Lin,[a,d] Meng Meng,[a,b,d] Cong Liu,[c] Kai Hao,*[c] Xuan Pang,[a,b,d] Huayu Tian *[a,b,c,d,e] and Xuesi Chen[a,b,d]

Received 29th June 2023,
Accepted 22nd July 2023

DOI: 10.1039/d3bm01088k

rsc.li/biomaterials-science

The emergence of nanocarriers has greatly improved the therapeutic efficacy of chemotherapeutic drugs. As emerging nanocarriers, covalent organic frameworks (COFs) have been increasingly used in biomedicine in recent years. However, due to their inherent chemical stability, existing COF nanocarriers hardly undergo *in vivo* degradation, which brings potential safety hazards to further applications. In this work, we introduce the azo bond into COFs. When the nanocarrier enters the cell, $^{\bullet}OH$ generated by the coordinated Fe response to the H_2O_2 in the cell will break the azo bond and cause the degradation of the framework structure, accelerating the release of internally loaded DOX to effectively realize tumor treatment. We verified the degradation ability of the materials by constructing model compounds, *in vitro* drug release, MTT assay and antitumor experiments. Compared with the control groups, the degradable COF accelerates the release of DOX and shows a stronger killing effect on 4T1 cells. Serum biochemical analysis and H&E sections of organs show good biocompatibility for both COFs and degradation products. This work provides a new idea for the design of biodegradable COFs *in vivo*, and greatly explores the potential application of COF materials in the biomedical field.

Introduction

Cancer is currently a major disease threatening human health, and traditional treatment methods still have certain limitations.[1] For example, although surgical treatment can be relatively direct to remove early lesions,[2] it is easy to relapse after surgery and is not suitable for metastatic and difficult-to-resect cancers. However, radiotherapy and chemotherapy have great therapeutic side effects,[3,4] which can easily affect the health of patients due to lack of specificity. Therefore, there is an urgent need to develop more targeted and effective treatments. Nanocarriers have received extensive attention from researchers in recent years for increasing the circulation time of drugs in the body,[5–7] increasing the enrichment at tumor sites, penetrating deeply into the tumor, and achieving effective drug release after tumor cell internalization, thus bringing great improvement to the therapeutic effect.

As an emerging organic porous material,[8–12] covalent organic frameworks (COFs) have attracted extensive attention from researchers not only because of their common characteristics of conventional nanocarriers[13–15] but also because of their many unique properties such as periodicity, crystallinity, porosity, stability and so on. When used as nanocarriers,[16–18] these properties allow COFs with a flexible design according to requirements to exhibit efficient encapsulation and transport of the guest molecule.

There have been many reports on the successful application of COFs in biomedicine,[19,20] but there are still some problems to be solved when they are applied: (1) controlled drug release.[13] The existing COF nanocarriers are still unable to use the characteristic signals of the tumor micro-environment as the stimulus source to construct a responsive drug delivery system, which can realize the targeted delivery of drugs at the tumor site. (2) *In vivo* degradability.[21,22] Most of the currently available COFs are not degradable *in vivo*; their good chemical stability also brings potential safety issues to their *in vivo*

[a]*Key Laboratory of Polymer Ecomaterials, Changchun Institute of Applied Chemistry, Chinese Academy of Sciences, Changchun 130022, China. E-mail: thy@xmu.edu.cn*
[b]*School of Applied Chemistry and Engineering, University of Science and Technology of China, Hefei 230026, China*
[c]*State Key Laboratory of Physical Chemistry of Solid Surfaces, College of Chemistry and Chemical Engineering, Xiamen University, Xiamen 361005, China. E-mail: kaihao@xmu.edu.cn*
[d]*Jilin Biomedical Polymers Engineering Laboratory, Changchun 130022, China*
[e]*Innovation Laboratory for Sciences and Technologies of Energy Materials of Fujian Province (IKKEM), Xiamen 361005, China*

†Electronic supplementary information (ESI) available. See DOI: https://doi.org/10.1039/d3bm01088k

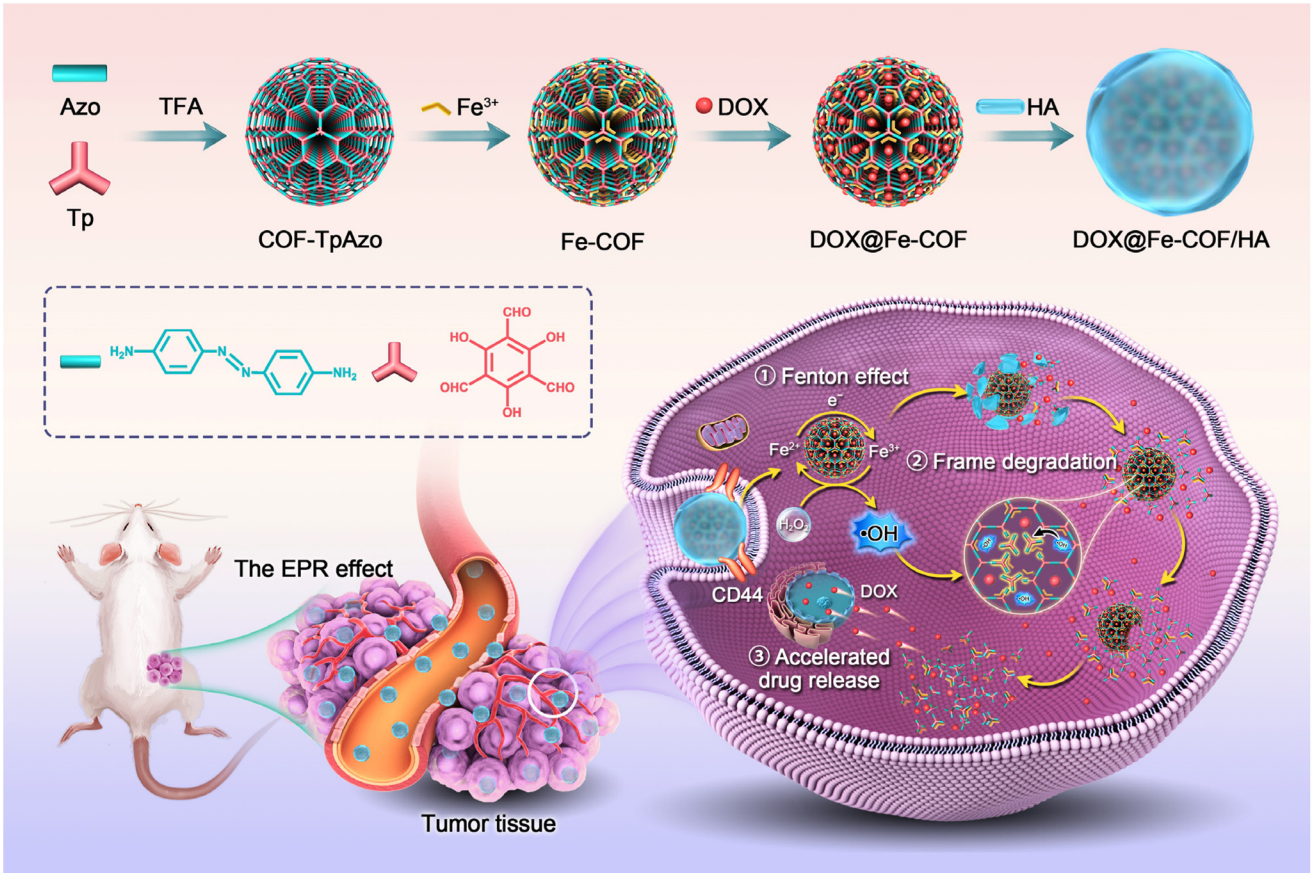

Scheme 1 Schematic illustrations of the formation of COF-TpAzo NPs and *in vivo* framework degradation for enhanced tumor therapy.

application. Therefore, COF nanocarriers for *in vivo* applications still need to be further improved.

To solve the above problems, we designed the work described in this paper, as shown in Scheme 1. Degradable COF-TpAzo was prepared by the covalent reaction of 1,3,5-triformylphloroglucinol (Tp) and 4,4′-azodianiline (Azo), and then coordinated iron ions, loaded doxorubicin (DOX), and masked hyaluronic acid (HA) to finally obtain an intelligent nano drug delivery system *in vivo*. After being enriched at the tumor site through the EPR effect,[23,24] the nano drug delivery system targeted and recognized the CD44 receptor on the tumor cell membrane.[25,26] After entering the cell, in response to the characteristic signal in the tumor cell with a high concentration of H_2O_2,[27,28] Fe ions produced the Fenton effect,[29–31] generating hydroxyl radicals, which broke the azo bond on the COF structure, resulting in the degradation of the COF carrier. At the same time, the release of doxorubicin was accelerated to achieve the killing of tumor cells.

The nanoplatform has the following characteristics: (1) the prepared COF NPs could accumulate at the tumor site by means of the EPR effect, and the encapsulated HA could respond to the CD44 receptor on the surface of tumor cells to achieve targeted delivery to tumor cells; (2) the $^{\bullet}OH$ generated by the Fenton effect in response to H_2O_2 at the tumor site could break the azo bond of the COF backbone,[32,33] resulting in the biodegradation of COF; (3) the degradation of the COF backbone accelerated the controlled release of DOX, enabling targeted drug delivery.

We characterized the structure and physicochemical properties of COFs in detail, evaluated the degradation properties of the materials at the material and cellular levels, and evaluated the antitumor properties of the materials in a 4T1 tumor-bearing mouse model. The small molecule degradation products did not cause significant toxicity in mice, indicating that this work is a meaningful attempt at degradable COFs, and this work has made a meaningful exploration in expanding the application of COFs in the field of biomedicine.

Experimental

Materials

4,4′-Azodianiline (Azo) was obtained from Shanghai Macklin Biochemical Co., Ltd (Shanghai, China). 1,3,5-Triformylphloroglucinol (Tp) was obtained from Zhengzhou JACS Chem Product Co., Ltd (Henan, China). Trifluoroacetic acid (TFA) was bought from Aladdin Biochemical Technology Co., Ltd (Shanghai, China). Polyvinylpyrrolidone (M_w = 40 000) was obtained from Energy Chemical (Anhui, China). 3,3′,5,5′-Tetramethylbenzidine (TMB) and $FeCl_3{\cdot}6H_2O$ were obtained

from J&K Chemicals (Beijing, China). DOX hydrochloride (DOX·HCl) was obtained from Meilun Biotechnology Corporation (Dalian, China). Hyaluronic acid (HA) was acquired from Freda (Shandong, China). Dulbecco's modified Eagle's medium (DMEM) and fetal bovine serum (FBS) were acquired from Gibco (Grand Island, USA). 4′,6-Diamidino-2-phenylindole dihydrochloride (DAPI) and methyl thiazolyl tetrazolium (MTT) were purchased from Sigma-Aldrich (St Louis, MO, USA). The other reagents were obtained from Sinopharm Chemical Reagent Co. Ltd, China. *N*,*N*′-Dimethylthiourea (DMTU) was bought from TCI Chemicals (Shanghai, China). All blood index assay kits were obtained from Nanjing Jiancheng Bioengineering Institute.

Murine 4T1 breast cancer cells were obtained from the cell bank of the Chinese Academy of Sciences (Shanghai, China). All cells were cultured in Dulbecco's modified Eagle's medium (DMEM) containing 10% fetal bovine serum. Cells were incubated at 37 °C under a humidified atmosphere containing 5% CO_2.

Animals

Female Balb/c mice (6–8 weeks, 18–22 g) were obtained from Vital River Company (Beijing, China). All animal procedures were performed in accordance with the Guidelines for Care and Use of Laboratory Animals of Northeast Normal University and approved by the Animal Ethics Committee of Northeast Normal University.

Synthesis and characterization of COF-TpAzo NPs

4,4′-Azodianiline (Azo) (0.045 mmol, 9.5 mg) and 1,3,5-triformylphloroglucinol (Tp) (0.03 mmol, 6.3 mg) were dissolved in 100 mL of dichloromethane (DCM) in a 250 mL round bottom flask at room temperature, separately, resulting in a transparent yellow and a colorless solution, respectively. Trifluoroacetic acid (TFA, 10 μl) was added to the Azo solution, followed by adding Tp solution, which turned the color of the solution from yellow to dark purple to wine red. Two hours after that, 20 mg of polyvinylpyrrolidone (PVP, M_w = 40 000) was added, resulting in the turbid solution being transformed into a transparent solution immediately. After stirring for 70 hours, the reaction mixture was concentrated under reduced pressure, and n-hexane was added to separate the COF nanoparticles from the solutions. After complete precipitation of all the COF nanospheres, the precipitate was collected and washed thoroughly with dimethylacetamide (DMAc) followed by dry acetone and isolated as a red powder after drying in an oven at 120 °C.

The zeta potential and size of materials were characterized using a zeta potential/BI-90Plus particle size analyzer (Brookhaven, USA). Fourier transform infrared (FT-IR) spectra were recorded on a Bruker VERTEX70 spectrometer. A PXRD study was performed using a wide-angle X-ray diffractometer (D8 ADVANCE, Bruker, Germany) using Cu-Kα radiation. 400 MHz solid state ^{13}C CP-MAS NMR spectra were obtained using a Bruker AVANCE III HD spectrometer. SEM images were obtained using a field emission scanning electron microscope (Zeiss Merlin FE-SEM). N_2 isotherms were measured on a volumetric analyzer (Autosorb iQ, Quantachrome, USA).

Preparation of Fe-COF NPs

10 mg of COF-TpAzo powder, 170 mg of $FeCl_3{\cdot}6H_2O$ and 5 mL of *N*,*N*-dimethylformamide (DMF) were added in a round bottom flask at 120 °C and refluxed overnight. The Fe-COF precipitate was collected and washed thoroughly with deionized water in order to remove residual $FeCl_3{\cdot}6H_2O$ in the system and isolated as a dark red powder after drying in an oven at 120 °C.

Preparation of DOX@Fe-COF NPs

Fe-COF NPs and DOX·HCl were dispersed in DMSO, and triethylamine was added to it to remove hydrochloride and then stirred for 0.5 h; then, the resultant product was dropped into water under stirring, the volume of which was two times that of DMSO, and the mixture was stirred overnight. The DOX@Fe-COF NPs were collected by centrifugation and washed three times with water. The DOX@Fe-COF NPs were soaked in DMSO and stirred overnight. After centrifugation, the DOX content in the supernatant was considered the total DOX content in DOX@Fe-COF NPs. After the concentration was determined by a UV-Vis absorption spectrum at 480 nm, DLE and DLC were calculated by comparing them with the standard curve:

$$\text{DLE (wt\%)} = (\text{weight of loaded drug/weight of feeding drug}) \times 100\%$$

$$\text{DLC (wt\%)} = (\text{weight of loaded drug/weight of NPs}) \times 100\%$$

The preparation process of DOX@COF NPs was similar.

X-ray photoelectron spectroscopy (XPS) data were collected using a Thermo Scientific ESCALAB 250 Multitechnique Surface Analysis system.

Preparation of DOX@Fe-COF/HA NPs

The DOX@Fe-COF NPs and HA were dissolved in deionized water with a weight ratio of 10 : 1 and stirred for 30 min. The mixed solution was centrifuged at 10 000 rpm for 10 min to obtain DOX@Fe-COF/HA NPs and washed with deionized water three times.

Preparation of the model compound

Tp (0.25 mmol, 52.5 mg), *P*-aminoazobenzene (2.5 mmol, 492.5 mg) and 50 mL of DCM were added in a round bottom flask at 70 °C and refluxed overnight. The yellow precipitate was washed with acetone three times and then centrifuged and dried in an oven to obtain the model compound.

Detection of ˙OH

Fe-COF NPs (1 mg mL^{-1}) and H_2O_2 (100 μM, consistent with the concentrations at tumor sites reported in the literature) were mixed in deionized water. A 0.2 mM TMB solution, which was employed as a chromogenic agent to display the ˙OH gene-

ration, was added to the system. The absorption peak changes of the samples at 650 nm were observed using a UV-visible spectrophotometer.

Drug release of DOX@Fe-COF

Considering that DOX loaded in DOX@Fe-COF NPs was in the form of non-hydrochloride, it was not a water-soluble drug, so we added 0.5% Tween 80 to the PB solution to facilitate drug release. 1 mg of DOX@Fe-COF NPs or DOX@COF NPs was added to a centrifuge tube, and 1 mL of release buffers with different pH values were added. The final concentration of H_2O_2 in the control group was 100 μM, which was the same as that in the tumor tissue. Three parallel groups were prepared, and the centrifuge tubes were placed in a constant temperature shaking box at 37 °C and shaken in the dark. The supernatant was centrifuged at different time points to measure the UV absorption intensity at 480 nm, and then 1 mL of release buffer was added with continued shaking. The final release efficiency was the cumulative result of all time points before this.

Cytotoxicity assay

The cytotoxicity of DOX@Fe-COF/HA was investigated by MTT assay. Briefly, 4T1 cells (8000 cells per well) were seeded in 96-well plates and incubated for 24 h (37 °C, 5% CO_2). After being treated with different groups, the cells were incubated again for 24 h before adding 20 μL of MTT. After incubation for 4 h, the medium and MTT were removed, and 150 μL of DMSO was added. Then, the absorption at 492 nm was measured by using a Bio-Read 680 microplate reader.

Cellular uptake

Cellular uptake capacity was explored using a CLSM and flow cytometry. In the CLSM experiment, 4T1 cells (3×10^5 cells per well) were seeded on cover glasses in 6-well plates and incubated for 24 h (37 °C, 5% CO_2). Then, 25 μg mL^{-1} DOX@Fe-COF/HA was added. After different incubation times, the medium was swapped with 4% paraformaldehyde and fixed at room temperature for 15 min after washing with PBS five times. Then, the cells were washed with PBS five times and stained with 1 mg mL^{-1} DAPI (2 μL per well). After washing with PBS again five times, the cover glasses were removed, immobilized on slides and sealed with glycerol for imaging using a CLSM (ZEISS LSM780, Germany). In the flow cytometry experiment, 4T1 cells were seeded in 6-well plates (3×10^5 cells per well) and incubated for 24 h (37 °C, 5% CO_2). Then, 25 μg mL^{-1} DOX@Fe-COF/HA was added. After incubation, the cells were digested at different time points with trypsin and washed with PBS two times and then re-dispersed in PBS buffer for detecting the fluorescence intensity of DOX using a flow cytometer (Guava Technologies).

Mouse tumor models

Six- to eight-week-old Balb/c mice (female) were purchased from Vital River Company (Beijing, China). To construct the 4T1 tumor model, 1×10^6 cells in 50 μL of PBS buffer were implanted into the right flank of each mouse by subcutaneous injection. *In vivo* experiments were performed when the tumor had reached 100 mm^3. All animal experiments were conducted following the guidelines of laboratory animals created by the Animal Care and Use Committee of Northeast Normal University.

Biodistribution of DOX@Fe-COF/HA NPs

200 μL of DOX@Fe-COF/HA NPs were intravenously injected into 4T1 tumor-bearing mice at a dose of 5 mg kg^{-1} DOX in NPs. Then, at 12 h and 24 h post-injection, the mice were sacrificed under anaesthesia, and the tumors and major organs were collected for fluorescence imaging using a Maestro In Vivo Imaging System (Cambridge Research & Instrumentation, Inc., USA).

Antitumor experiment

When the tumor volume was 100 mm^3, 4T1 tumor-bearing Balb/c mice were casually allocated into four groups (n = 5), including PBS, Fe-COF/HA, DOX@Fe-COF/HA + DMTU, and DOX@Fe-COF/HA. DOX@Fe-COF/HA NPs (200 μL) were intravenously injected at a DOX dose of 5 mg kg^{-1} every two days. 25 μL of 50 μM DMTU was intratumorally injected at 12 h before COF NP injection. The body weight and tumor volume of mice of all the groups were measured every two days. The tumor volume was calculated according to the equation $a/2 \times b^2$ (a is the longer diameter, and b is the shorter diameter). The mice were sacrificed after 14 days of treatment to collect the major organs and tumors, which were further stained with hematoxylin and eosin (H&E) and TdT-mediated dUTP Nick-End Labeling (TUNEL).

Statistical analysis

Data analysis was performed using Microsoft Excel and GraphPad Prism 8 software. The data are presented as mean ± s.d. All of the statistical analyses were compared by Student's t-test. ($^*p < 0.05$ was considered statistically significant. $^{**}p < 0.01$ and $^{***}p < 0.001$ were considered extremely significant. "ns" indicated no significant differences.)

Results and discussion

Preparation and characterization of COF-TpAzo

COF-TpAzo nanoparticles were synthesized using 4,4′-azodianiline (**Azo**) and 1,3,5-triformylphloroglucinol (**Tp**) in dichloromethane solvent according to the method previously reported by Banerjee,[34] as shown in Fig. 1A. According to the literature, the particle size or the shape of COF-TpAzo would be affected by the amount of catalyst trifluoroacetic acid added to the system and the time or temperature of the synthesis. After many attempts (Table S1, Fig. S1 and S2†), we finally determined the most suitable synthesis conditionsthat could be used to synthesize COF NPs with good crystallinity of the particle size for further use. The nanoparticles were subsequently collected by centrifugation. Fourier transform infrared (FT-IR)

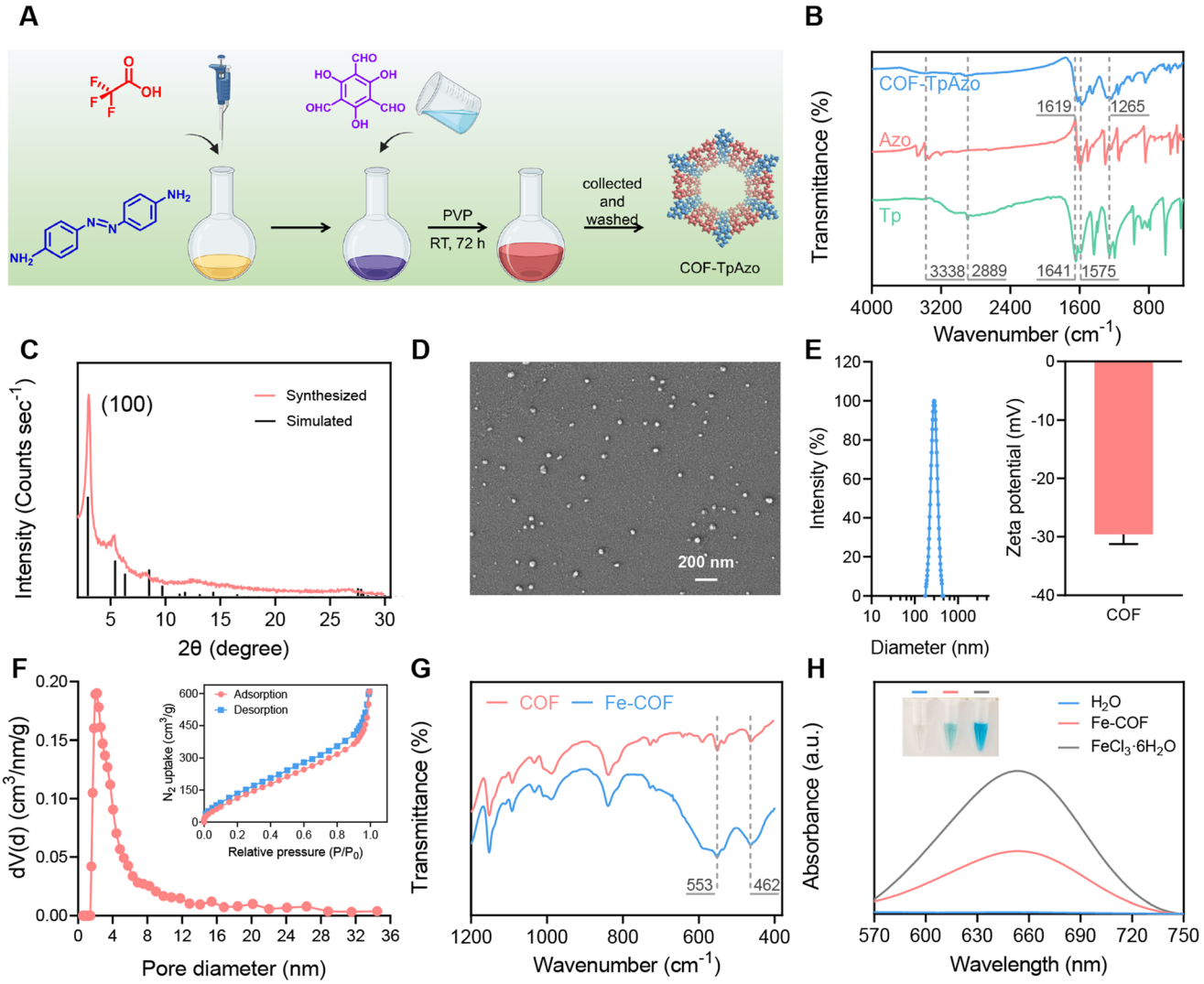

Fig. 1 Synthetic route and characterization results. (A) Synthetic route to COF-TpAzo. (B) FT-IR spectra of COF-TpAzo, Tp monomer, and Azo monomer. (C) Comparison of the measured and simulated PXRD patterns of COF-TpAzo. (D) SEM images of COF-TpAzo (scale bar, 200 nm). (E) DLS result and zeta potential result of COF-TpAzo. (F) Pore size distribution of COF-TpAzo using the DFT method. The inset is the N_2 isotherm of COF-TpAzo. (G) FT-IR spectra of Fe-COF and COF-TpAzo. (H) UV-visible absorption spectra of TMB incubated with different groups to verify the $^{\bullet}OH$ generation. The inset is a digital photograph of the groups.

results in Fig. 1B show that after the reaction, the characteristic peaks of amino groups (–N–H) on Azo at 3338 cm^{-1}, and the characteristic peaks of aldehyde groups on Tp at 1641 cm^{-1} and 2889 cm^{-1} decreased in absorption. The absorption peaks of COFs at 1619 cm^{-1} (–C═O), 1575 cm^{-1} (–C═C) and 1265 cm^{-1} (–C–N) were generated, implying that the framework structure of nanoparticles was obtained by forming imine bonds between Azo monomer and Tp monomer, which proved the successful synthesis of COF-TpAzo. The powder X-ray diffraction (PXRD) spectra in Fig. 1C show that the experimental patterns were in good agreement with the eclipsed-AA stacking models simulated by the references.[36] The high-intensity peak at 3 degrees, which was attributed to their (100) plane diffractions, indicated the high crystallinity of the COF NPs.

The synthesized nanoparticles show a uniform particle size of around 40 nm under scanning electron microscopy (SEM) (Fig. 1D). We also provided SEM images with larger magnification to observe the morphology of COFs (Fig. S3†). DLS and zeta potential results are shown in Fig. 1E. The particle size of COF NPs was 289 nm ± 7.1 nm, and the zeta potential was −29.5 mV. We also verified the permanent porosity and architectural rigidity of the COF nanoparticles from their N_2 adsorption analysis at 77 K. The results in Fig. 1F show excellent porosity with a surface area of around 503 $m^2\ g^{-1}$ and a pore size of 2.1 nm for COF-TpAzo, which was further evidence of the successful synthesis of COF NPs. The results of solid-state NMR were also in line with the literature (Fig. S4†).

Subsequently, Fe coordination was performed on COF NPs. COF NPs and $FeCl_3{\cdot}6H_2O$ were refluxed in DMF solution at

120 °C for 24 h, and then the Fe-COF NPs were collected by centrifugation. As shown in Fig. 1G and S5,† we used FT-IR, X-ray photoelectron spectroscopy (XPS) and inductively coupled plasma-mass spectrometry (ICP-MS) to characterize the Fe-COF nanoparticles. The infrared absorption peaks of coordinated Fe at 553 cm^{-1} and 462 cm^{-1}, as well as the characteristic absorption peak at 711 eV in the XPS spectrum, indicated the successful coordination of Fe. ICP-MS results showed that the Fe content in Fe-COF was about 8%. Thermogravimetric analyses of COF-TpAzo under an N_2 atmosphere (Fig. S6)† indicated that COF-TpAzo is thermally stable up to ~450 °C. The curve of Fe-COFs was almost identical to that of COFs. This indicated that Fe coordination had no significant effect on the thermodynamic stability of COFs. Then, the Fenton effect generating ability of Fe-COFs was verified by 3,3′,5,5′-tetramethylbenzidine (TMB).[27] TMB could respond to hydroxyl radicals ($^{\bullet}OH$) in the Fenton reaction, resulting in blue coloration. We added TMB and H_2O_2 to Fe-COF and $FeCl_3{\cdot}6H_2O$ solutions, respectively, and measured the treated solutions by UV-Vis absorption spectroscopy. The results in Fig. 1H show that after the addition of Fe-COF and $FeCl_3{\cdot}6H_2O$ solutions, the originally colorless TMB and H_2O_2 mixed solution became visibly blue to the naked eye and produced the same absorption at 650 nm. The results showed that Fe-COFs had the ability to generate $^{\bullet}OH$ by the Fenton reaction with H_2O_2, which provided the possibility for subsequent COF degradation.

The degradability of Fe-COFs

Afterwards, we verified the degradability of the synthesized Fe-COFs. Considering the high molecular weight and complex structure of COFs, it was difficult to directly characterize the structural changes, which brings some obstacles to the verification of the degradability of COFs. Therefore, we designed and synthesized a model compound (MC) (2,4,6-tris(((4-(phenyldiazenyl)phenyl)amino)methylene)cyclohexane-1,3,5-trione) with the same azo bond structure of COF-TpAzo using a Tp monomer and an azobenzene monomer containing only one amino group to assist in verifying the degradation properties of Fe-COFs (Fig. S7†). The mass spectrometry (MS) results in Fig. 2C indicate the successful synthesis of the MC. It was then treated with Fe^{3+} and H_2O_2, and the reaction system was monitored by UV-Vis absorption spectroscopy. As shown in Fig. 2B, the results showed that the double peak absorption of the azo bond at 461 nm and 496 nm gradually weakened with the prolongation of treatment time, initially demonstrating the possibility that the azo bond of the MC was cleaved in response to H_2O_2.

Afterwards, we treated Fe-COFs and the MC with H_2O_2, while the MC was additionally treated with Fe^{3+}, and then characterized the two reaction systems by MS. The results in Fig. 2C show that after the treatment of the MC, in addition to the peak of the MC, three new peaks appeared in the system. Two of these peaks, 494.6 and 522.6, were completely coincident with the MS results of the Fe-COF system treated with H_2O_2, verifying that the degradation mechanism of Fe-COFs was similar to that of the MC, in which azo bonds played an important role in response to H_2O_2, which were speculated as the main degradation products of Fe-COFs or MC. According to the literature,[32,33] when the azo bond reacts with H_2O_2, the two ends would undergo oxidation and reduction reactions to generate the nitroso (–NO)-containing oxidation products and amino ($-NH_2$)-containing reduction products, respectively. Therefore, we proposed that the structural formulas of the two degraded products were as shown in Fig. 2A, in which case the molecular weights agree with the MS results. So far, we had completed the verification of the degradability of Fe-COFs; there was a chance to degrade into small molecules, and the degradation products **1** and **2** were possible degradation products,[32,33] and we deduced that the degradation was caused by the Fenton effect, so it could be inferred that Fe-COFs are biodegradable in the presence of H_2O_2 at the tumor site.

Preparation of DOX@Fe-COF NPs and their drug release ability

Next, we explored the drug loading capacity of Fe-COFs, as shown in Fig. 2D. After mixing DOX and Fe-COFs with different mass ratios, we detected the loading content in Fe-COFs by UV-Vis spectroscopy. The results showed that the highest loading efficiency was accomplished when the masses of DOX and Fe-COFs were equal, so we selected equal masses of DOX and Fe-COFs for loading to obtain DOX@Fe-COF nanoparticles. At this point, the loading capacity of DOX@Fe-COF was 20%. We also used the same synthesis method to synthesize DOX@COF at a mass ratio of 1/1 for comparison. Considering that the Fe atoms also occupy part of the pore volume of COFs after coordination, there was also a slight reduction in the drug loading capacity (Fig. S9†).

After the loading of DOX, we evaluated the drug release ability of DOX@COF and DOX@Fe-COF and compared the difference with or without H_2O_2. It could be seen from Fig. 2E and S10† that the release amount of DOX@COF had almost no change before and after the addition of H_2O_2. However, the release capacity of DOX@Fe-COF was significantly increased under the H_2O_2 conditions. Combined with the previous experimental results, we inferred that the Fenton effect was the key factor in the degradation of COF bonds. This property was beneficial for us to trigger controlled release *in vivo*.

Cytotoxicity of DOX@Fe-COF NPs

Then, the verification of cytotoxicity at the cellular level was performed. As shown in Fig. 2F, trace amounts of Fe in Fe-COFs did not affect cell viability. Even a high concentration of 100 μg mL^{-1} did not cause significant cell killing, indicating that Fe-COFs had good biocompatibility. The cytotoxicity of DOX@Fe-COFs loaded with DOX was then evaluated. As shown in Fig. 2G, the cytotoxicity also increased with increasing material concentration. 25 μg mL^{-1} DOX@Fe-COFs could directly reduce the cell viability to 40%. After the addition of H_2O_2, the cell viability of each concentration of material could be further reduced, resulting from more release of DOX. Calculation of IC50 of DOX@Fe-COFs with and without H_2O_2 is shown in Fig. S11.† Considering the small effect of H_2O_2

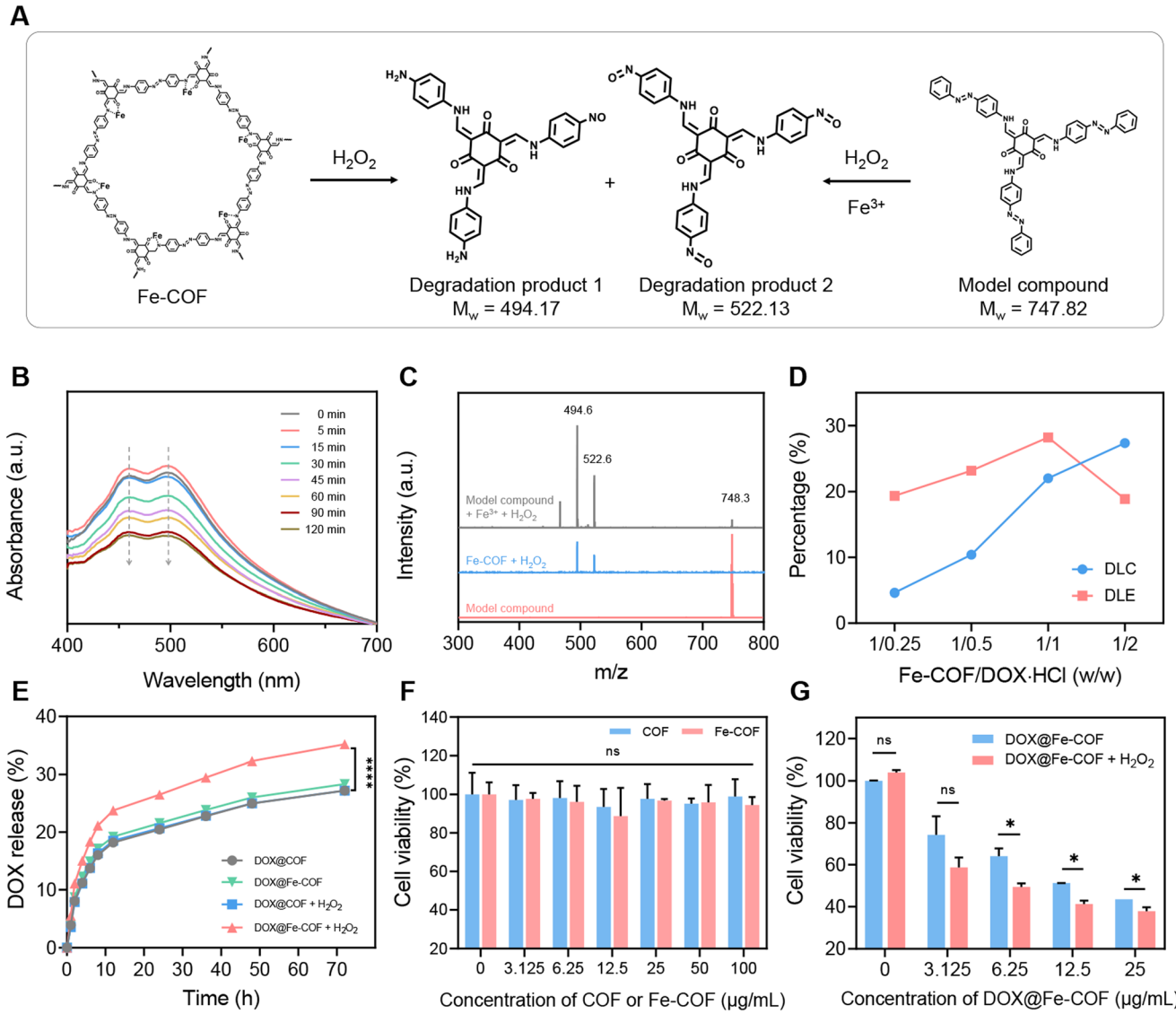

Fig. 2 Verification of degradability of an Fe-COF. (A) A possible degradation mechanism of Fe-COF and model compounds that we inferred. (B) Change of model compound UV-vis absorption spectra with time, when H_2O_2 and Fe^{3+} were added. (C) Mass spectra of the model compound, Fe-COF + H_2O_2, and model compound + Fe^{3+} + H_2O_2. (D) The loading efficiency and loading content of DOX@Fe-COFs varied with the mass ratios of DOX and Fe-COFs, which were detected by the UV-vis spectrum. (E) DOX release profiles from NPs in PB (pH = 6.8) with and without H_2O_2. (F) The cell cytotoxicity of Fe-COF NPs, indicating the biosafety of Fe-COF NPs. (G) The cell cytotoxicity of DOX@Fe-COF NPs with and without H_2O_2. The concentration of H_2O_2 added was 100 μM. Data are presented as the mean ± SD (n = 3). Significant differences were assessed using a t test (*p < 0.05, **p < 0.01, ***p < 0.001).

itself on the cell viability, we could conclude that the enhanced killing effect on tumor cells stemmed from the degradation of Fe-COFs after adding H_2O_2, thus accelerating the internally loaded DOX release. Fe-COFs had almost no therapeutic effect on the tumor, and we speculated that the Fenton effect produced was not enough to inhibit tumor growth.

Cellular uptake and *in vivo* distribution of DOX@Fe-COF NPs

The cellular uptake of 4T1 cells incubated with DOX@Fe-COF NPs at different treatment times was observed using a confocal laser scanning microscope (CLSM), as shown in Fig. 3A. The results showed that the fluorescence co-localization of the nucleus and DOX was observed for about 6 h, indicating that DOX@Fe-COF NPs took about 6 h to complete the endocytosis.

To increase the stability of nanoparticles, we masked HA onto DOX@Fe-COF nanoparticles (Fig. S12 and S13†). At the same time, the specific binding ability between HA molecules and the highly expressed CD44 receptor on the surface of tumor cells also contributes to improving the targeting of nanoparticles to tumor cells (Fig. S14†).

The *in vivo* distribution of the materials was studied with *in vivo* imaging equipment, and DOX@Fe-COF/HA was administered by tail vein injection. Free DOX was also studied as a control group. In addition, intratumoral injection of

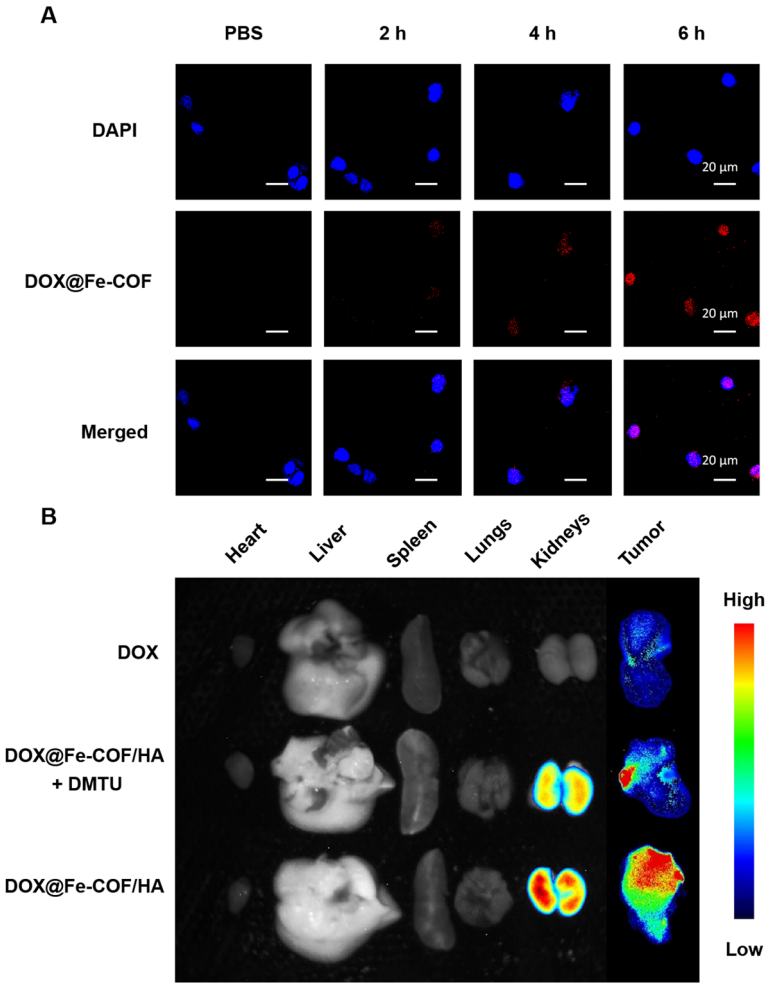

Fig. 3 Endocytosis and biodistribution. (A) The CLSM images of 4T1 tumor cells incubated with DOX@Fe-COF NPs for 2 h, 4 h, and 6 h. Scale bar: 20 μm. (B) The fluorescence images of mouse organs and tumors after tail vein injection of DOX@Fe-COF/HA NPs for 12 h and 24 h.

N,*N*′-dimethylthiourea (DMTU) was used to deplete H_2O_2 at the tumor site for comparison with DOX@Fe-COF/HA without additional treatment to verify the effect of intratumoral H_2O_2 on COF degradation.[35] After a certain period of tail vein injection, the organs and tumors of the 4T1 tumor-bearing mice in each group were dissected for fluorescence intensity observation. The quantification results of the normalized fluorescence signal are shown in Fig. S15.†

The results in Fig. 3B show that 12 hours after the tail vein injection of free DOX, there was only a little fluorescence in the tumor, but almost no fluorescence was observed in other organs. This showed that free DOX stayed in the body only for a short time and was quickly eliminated.

However, both DOX@Fe-COF/HA and DOX@Fe-COF/HA + DMTU groups had significant intratumoral accumulation 12 h after tail vein injection, but the intratumoral DMTU group had less accumulation in tumors. That may be because the lack of H_2O_2 slowed down the degradation of the COF and hindered the release of DOX. It could be concluded that in the process of delivering DOX into cells by DOX@Fe-COF/HA nanoparticles, H_2O_2 helped to release, which increased the degradation of COFs and provided a basis for a better antitumor effect.

Antitumor effect *in vivo*

We then designed the treatment protocol shown in Fig. 4A to verify the *in vivo* treatment and degradation effects of the nanoparticles. Twenty mice were seeded with 4T1 tumors, and each was injected with approximately 1 million 4T1 cells. After 7 days, the mice were randomly divided into 4 groups with 5 mice in each group, namely G1: the PBS group, G2: the Fe-COF/HA group, G3: the DOX@Fe-COF/HA + DMTU group, and G4: the DOX@Fe-COF/HA group. Likewise, DMTU was injected intratumorally one day before nanoparticle administration to deplete H_2O_2 at the tumor sites to validate the nature of COF-responsive degradation. When the tumor volume reached approximately 100 mm^3, tail vein injection of the nanoparticles was performed.

The results in Fig. 4B showed that the tumor growth trend of the Fe-COF/HA group and PBS group were almost identical, which meant that Fe-COF/HA had almost no inhibitory effect on tumor growth. We conjectured that the coordinated Fe was

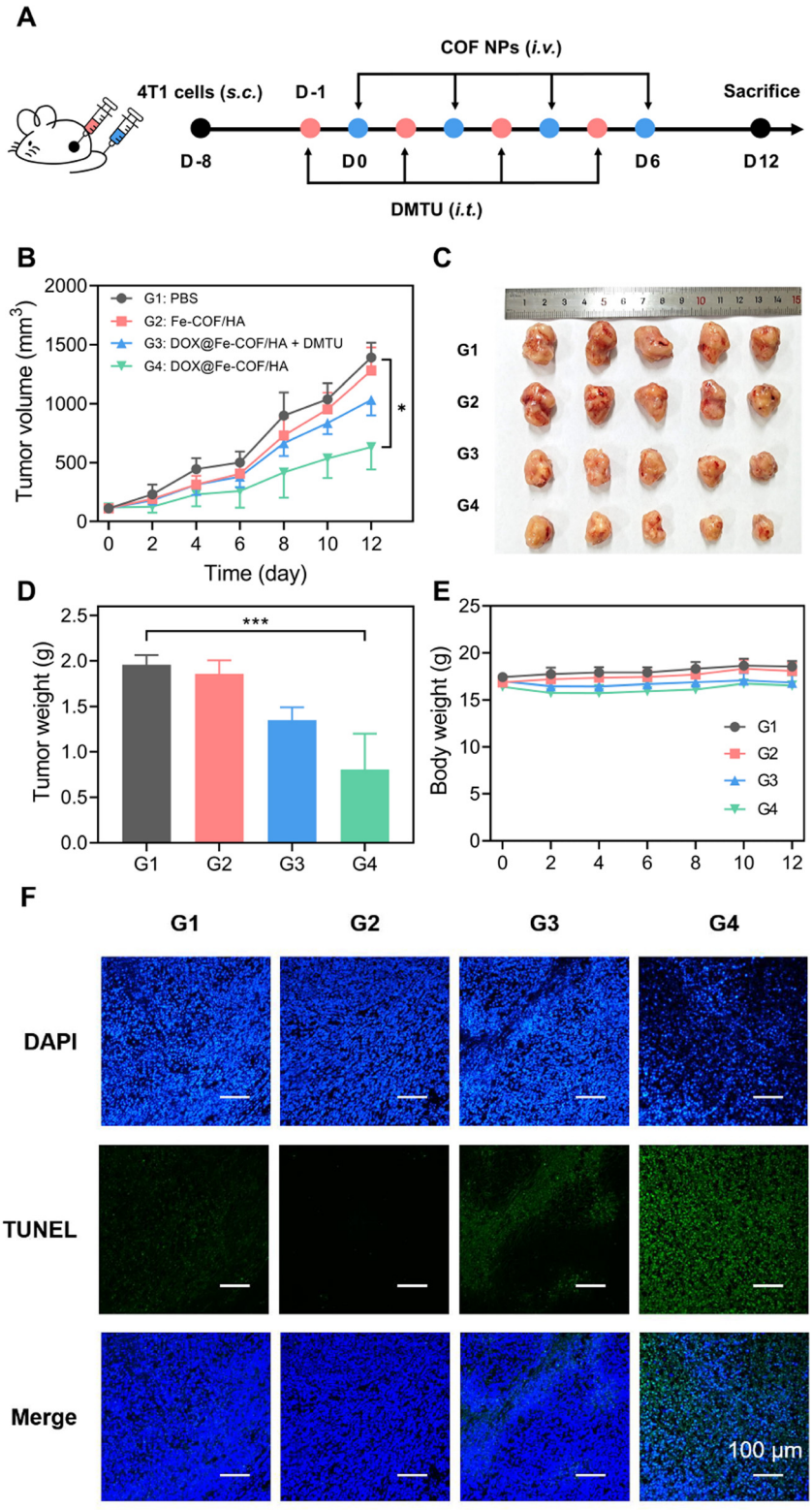

Fig. 4 Antitumor effect *in vivo*. (A) The therapeutic schedule of 4T1 tumor-bearing mice. DMTU was only used in the DOX@Fe-COF/HA + DMTU-treated group, and it was injected 12 h before injecting DOX@Fe-COF/HA NPs. (B) Tumor growth curves of the mice of different groups. (C and D) Tumor photograph and tumor weight of different groups. (E) The body weight change curves of different groups. (F) TUNEL staining images of excised tumor tissues. G1: the PBS group, G2: the Fe-COF/HA group, G3: the DOX@Fe-COF/HA + DMTU group, and G4: the DOX@Fe-COF/HA group. Scale bar: 100 μm. Data are presented as the mean ± SD (n = 5). Significant differences were assessed using a t test (*p < 0.05, **p < 0.01, ***p < 0.001).

too little and the generated ·OH was too little to produce any killing effect, in agreement with the cytotoxic results.

In contrast, the DOX@Fe-COF/HA group provided the best therapeutic effect, significantly inhibiting tumor growth, where the inhibition rate exceeds 50%, significantly outperforming the DOX@Fe-COF/HA + DMTU group. We speculated that the presence of H_2O_2 at the tumor site, which was essential for the degradation of Fe-COFs, enhanced the therapeutic effect by accelerating the release of internally loaded DOX. When H_2O_2 was consumed with DMTU, the degradation of Fe-COFs slowed down, which in turn slowed down the release of DOX, thus making the treatment less effective. The results of Fig. 4C and D were also consistent with the above results. In addition, the TUNEL staining results in Fig. 4F also showed that the DOX@Fe-COF/HA group exhibited the highest fluorescence intensity, that is, the most apoptosis occurred compared to the other groups, which was in line with the trend in our other treatment results.

Considering the above treatment results, we further validated the degradability of Fe-COFs *in vivo*, with H_2O_2 being an important external factor. As high H_2O_2 concentration was an important marker of the tumor site, the treatment results also illustrated the responsiveness of Fe-COFs to the tumor site.

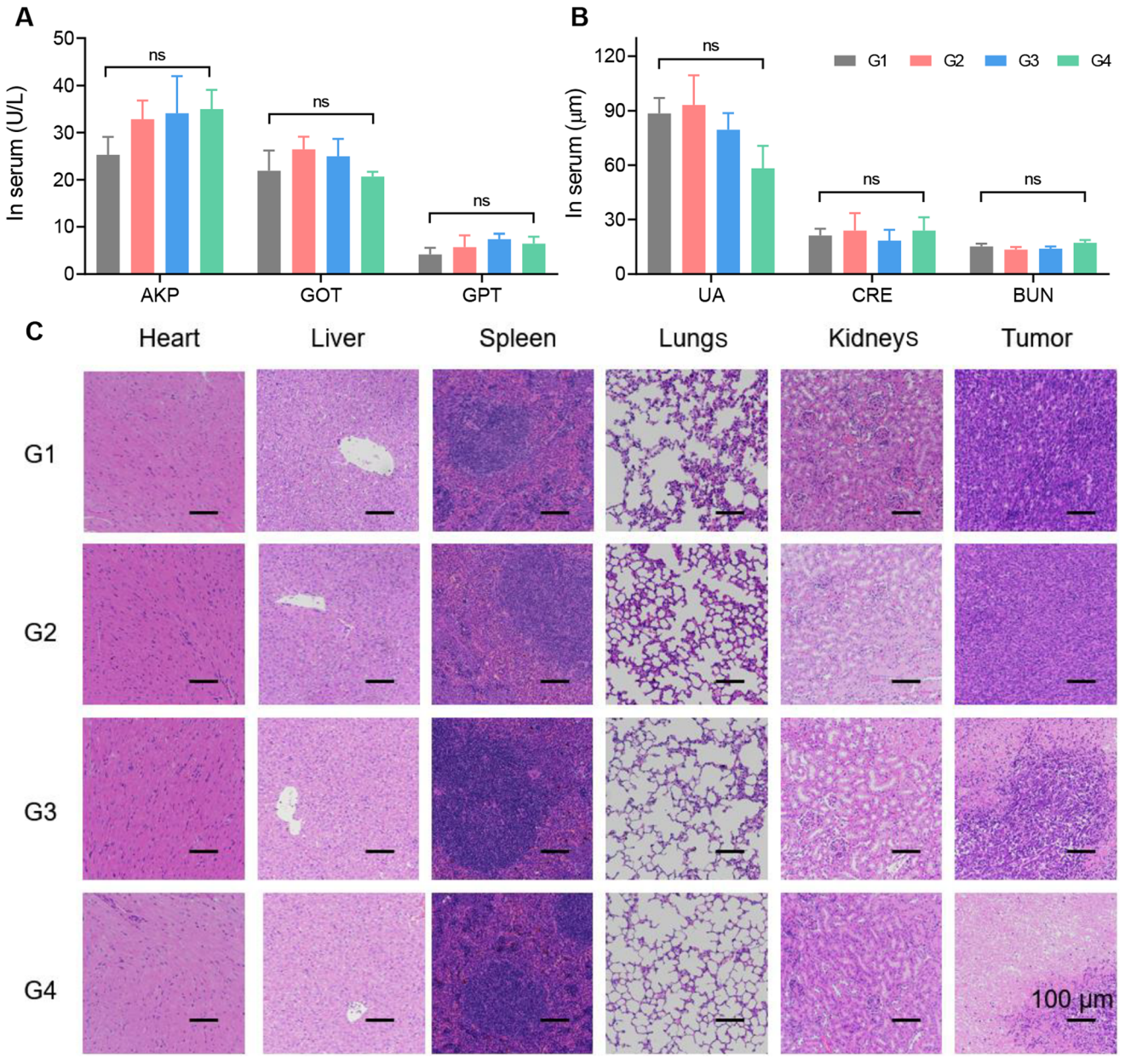

Fig. 5 Biosafety assessment. (A and B) The detection of liver and kidney functional markers in the serum of mice of different groups. (C) H&E staining images of excised tumor tissues. G1: the PBS group, G2: the Fe-COF/HA group, G3: the DOX@Fe-COF/HA + DMTU group, and G4: the DOX@Fe-COF/HA group. Scale bar: 100 μm. Data are presented as the mean ± SD (n = 5). Significant differences were assessed using a t test (*p < 0.05, **p < 0.01, ***p < 0.001).

Biosafety of DOX@Fe-COF/HA NPs

Finally, we monitored the *in vivo* safety of the materials. The biosafety of the material itself, as well as the biosafety of degradation products, were our main concerns.

As shown in Fig. 4E, the changes in the body weight of the mice after all four treatments were negligible. For the DOX@Fe-COF/HA group, it was seen that the material had good biocompatibility during the treatment process as in the other groups. In addition, blood biochemical indexes were measured. AKP, GOT and GPT were used to measure the liver function of the mice, and UA, CRE and BUN were used to measure the kidney function. The results in Fig. 5A and B show that the differences in the measured values of each group were very small, and the indicators were consistent with no significant difference, indicating that the liver and kidney functions of the mice were not affected, and the material had no obvious biological toxicity. In addition, we studied the organ sections of each group, and the H&E results showed that there was no obvious change in the organs of each group (Fig. 5C). In the sections of the tumor sites in each group, the tumor cells in the G4 group were significantly reduced, showing the highest number of apoptotic cells, which once again proved that the therapeutic effect of the DOX@Fe-COF/HA group was best. It could be concluded that the DOX@Fe-COF/HA group had the best therapeutic effect and higher biological safety.

Conclusions

In summary, our method prepared a 40 nm large COF nanoparticle under a scanning electron microscope for DOX loading, which could achieve 20% drug loading, and Fe-COF NPs could respond to high concentrations of H_2O_2 at the tumor site, producing $^{\bullet}OH$, which broke the azo bond, thereby achieving the degradation of the framework. After externally shielding with HA, the accumulation in the tumor could be achieved, thereby realizing the controllable release of DOX in the tumor microenvironment, helping us to achieve a high tumor inhibition efficiency in the 4T1 tumor model, which could reach more than 50%. Serum biochemistry and H&E sections showed that COF NPs and degradation products did not show obvious toxic and side effects on the physiological functions of mice, indicating that COF NPs possess good *in vivo* safety. This work will expand the application of COFs in the field of antitumor research. In the future, we will continue to enrich the types of degradable chemical bonds and explore COF nanoparticles that are more suitable for clinical applications.

Author contributions

Tong Li: conceptualization, methodology, validation, investigation, and writing – original draft. Dianwei Wang: conceptualization, methodology, validation, software, and investigation. Zhaopei Guo: methodology and software. Lin Lin: investigation and funding acquisition. Meng Meng: software and investigation. Cong Liu: investigation and funding acquisition. Kai Hao: methodology, validation, writing – review & editing, and supervision. Xuan Pang: supervision. Huayu Tian: methodology, funding acquisition, writing – review & editing, and supervision. Xuesi Chen: funding acquisition and supervision. The manuscript was written through contributions of all authors. All authors have given approval to the final version of the manuscript.

Conflicts of interest

The authors declare no competing financial interest.

Acknowledgements

The authors are thankful to the National Key Research and Development Program of China (2021YFB3800900), the National Natural Science Foundation of China (51925305, 51873208, 51833010, 51803210 and 52203189), and the Talent Cultivation Project Funds for the Innovation Laboratory for Sciences and Technologies of Energy Materials of Fujian Province (HRTP-[2022]52).

References

1 X. Li, X. Cai, Z. Zhang, Y. Ding, R. Ma, F. Huang, Y. Liu, J. Liu and L. Shi, Mimetic Heat Shock Protein Mediated Immune Process to Enhance Cancer Immunotherapy, *Nano Lett.*, 2020, **20**, 4454–4463.

2 M. Morrow, J. White, J. Moughan, J. Owen, T. Pajack, J. Sylvester, F. Wilson and D. Winchester, Factors Predicting the Use of Breast-Conserving Therapy in Stage I and II Breast Carcinoma, *J. Clin. Oncol.*, 2001, **19**, 2254–2262.

3 W. A. Volkert and T. J. Hoffman, Therapeutic Radiopharmaceuticals, *Chem. Rev.*, 1999, **99**, 2269–2292; H. Chen, F. Tung, M. Chen and T. Liu, A magnetic vehicle realized tumor cell-targeted radiotherapy using low-dose radiation, *J. Controlled Release*, 2016, **22.6**, 182–192.

4 Y. Zhao, X. Hou, J. Chai, Z. Zhang, X. Xue, F. Huang, J. Liu, L. Shi and Y. Liu, Stapled Liposomes Enhance Cross-Priming of Radio-Immunotherapy, *Adv. Mater.*, 2022, **34**, 2107161.

5 Z. Li, C. Xiao, T. Yong, Z. Li, L. Gan and X. Yang, Influence of nanomedicine mechanical properties on tumor targeting delivery, *Chem. Soc. Rev.*, 2020, **49**, 2273–2290.

6 X. Zhang, D. Wang, X. Wu, Y. Zhao, X. Li, R. Ma, F. Huang and L. Shi, "Spear and shield in one" nanochaperone enables protein to navigate multiple biological barriers for enhanced tumor synergistic therapy, *Biomater. Sci.*, 2022, **10**, 3575–3584.

7 J. Wang, S. Shen, J. Li, Z. Cao and X. Yang, Precise Depletion of Tumor Seed and Growing Soil with Shrinkable Nanocarrier for Potentiated Cancer Chemoimmunotherapy, *ACS Nano*, 2021, **15**, 4636–4646.
8 Q. Guan, L. L. Zhou, W. Y. Li, Y. A. Li and Y. B. Dong, Covalent Organic Frameworks (COFs) for Cancer Therapeutics, *Chem. – Eur. J.*, 2020, **26**, 5583–5591.
9 V. S. Vyas, M. Vishwakarma, I. Moudrakovski, F. Haase, G. Savasci, C. Ochsenfeld, J. P. Spatz and B. V. Lotsch, Exploiting Noncovalent Interactions in an Imine-Based Covalent Organic Framework for Quercetin Delivery, *Adv. Mater.*, 2016, **28**, 8749–8754.
10 S. B. Wang, Z. X. Chen, F. Gao, C. Zhang, M. Z. Zou, J. J. Ye, X. Zeng and X. Z. Zhang, Remodeling extracellular matrix based on functional covalent organic framework to enhance tumor photodynamic therapy, *Biomaterials*, 2020, **234**, 119772.
11 C. Qian, Q. Y. Qi, G. F. Jiang, F. Z. Cui, Y. Tian and X. Zhao, Toward Covalent Organic Frameworks Bearing Three Different Kinds of Pores: The Strategy for Construction and COF-to-COF Transformation via Heterogeneous Linker Exchange, *J. Am. Chem. Soc.*, 2017, **139**, 6736–6743.
12 J. Feng, Y. J. Zhang, S. H. Ma, C. Yang, Z. P. Wang, S. Y. Ding, Y. Li and W. Wang, Fused-Ring-Linked Covalent Organic Frameworks, *J. Am. Chem. Soc.*, 2022, **144**, 6594–6603.
13 G. Zhang, X. Li, Q. Liao, Y. Liu, K. Xi, W. Huang and X. Jia, Water-dispersible PEG-curcumin/amine-functionalized covalent organic framework nanocomposites as smart carriers for in vivo drug delivery, *Nat. Commun.*, 2018, **9**, 2785–2796.
14 F. Benyettou, G. Das, A. R. Nair, T. Prakasam, D. B. Shinde, S. K. Sharma, J. Whelan, Y. Lalatonne, H. Traboulsi, R. Pasricha, O. Abdullah, R. Jagannathan, Z. Lai, L. Motte, F. Gandara, K. C. Sadler and A. Trabolsi, Covalent Organic Framework Embedded with Magnetic Nanoparticles for MRI and Chemo-Thermotherapy, *J. Am. Chem. Soc.*, 2020, **142**, 18782–18794.
15 D. Dutta, J. Wang, X. Li, Q. Zhou and Z. Ge, Covalent Organic Framework Nanocarriers of Singlet Oxygen for Oxygen-Independent Concurrent Photothermal/Photodynamic Therapy to Ablate Hypoxic Tumors, *Small*, 2022, 2202369.
16 Q. Fang, J. Wang, S. Gu, R. B. Kaspar, Z. Zhuang, J. Zheng, H. Guo, S. Qiu and Y. Yan, 3D Porous Crystalline Polyimide Covalent Organic Frameworks for Drug Delivery, *J. Am. Chem. Soc.*, 2015, **137**, 8352–8355.
17 S. Liu, C. Hu, Y. Liu, X. Zhao, M. Pang and J. Lin, One-Pot Synthesis of DOX@Covalent Organic Framework with Enhanced Chemotherapeutic Efficacy, *Chem. – Eur. J.*, 2019, **25**, 4315–4319.
18 L. Bai, S. Z. Phua, W. Q. Lim, A. Jana, Z. Luo, H. P. Tham, L. Zhao, Q. Gao and Y. Zhao, Nanoscale covalent organic frameworks as smart carriers for drug delivery, *Chem. Commun.*, 2016, **52**, 4128–4131.
19 D. Wang, L. Lin, T. Li, M. Meng, K. Hao, Z. Guo, J. Chen, H. Tian and X. Chen, Etching Bulk COFs into Nanoparticles of Uniform and Controllable Size by the Molecular Exchange Etching Method for Sonodynamic and Immune Combination Antitumor Therapy, *Adv. Mater.*, 2022, **34**, 2205924.
20 K. Hao, Z. Guo, L. Lin, P. Sun, Y. Li, H. Tian and X. Chen, Covalent organic framework nanoparticles for anti-tumor gene therapy, *Sci. China: Chem.*, 2021, **64**, 1235–1241.
21 Y. Shi, S. Liu, Y. Liu, C. Sun, M. Chang, X. Zhao, C. Hu and M. Pang, Facile Fabrication of Nanoscale Porphyrinic Covalent Organic Polymers for Combined Photodynamic and Photothermal Cancer Therapy, *ACS Appl. Mater. Interfaces*, 2019, **11**, 12321–12326.
22 X. Tong, S. Gan, J. Wu, Y. Hu and A. Yuan, A nano-photosensitizer based on covalent organic framework nanosheets with high loading and therapeutic efficacy, *Nanoscale*, 2020, **12**, 7376–7382.
23 B. Liu, Y. Bian, S. Liang, M. Yuan, S. Dong, F. He, S. Gai, P. Yang, Z. Cheng and J. Lin, One-Step Integration of Tumor Microenvironment-Responsive Calcium and Copper Peroxides Nanocomposite for Enhanced Chemodynamic/Ion-Interference Therapy, *ACS Nano*, 2022, **16**, 617–630.
24 Y. Qin, F. Tong, W. Zhang, Y. Zhou, S. He, R. Xie, T. Lei, Y. Wang, S. Peng, Z. Li, J. Leong, H. Gao and L. Lu, Self-Delivered Supramolecular Nanomedicine with Transformable Shape for Ferrocene-Amplified Photodynamic Therapy of Breast Cancer and Bone Metastases, *Adv. Funct. Mater.*, 2021, **31**, 2104645.
25 L. Huang, J. Liu, F. Gao, Q. Cheng, B. Lu, H. Zheng, H. Xu, P. Xu, X. Zhang and X. Zeng, A dual-responsive, hyaluronic acid targeted drug delivery system based on hollow mesoporous silica nanoparticles for cancer therapy, *J. Mater. Chem. B*, 2018, **6**, 4618–4629.
26 M. Y. Kwon, C. Wang, J. H. Galarraga, E. Pure, L. Han and J. A. Burdick, Influence of hyaluronic acid modification on CD44 binding towards the design of hydrogel biomaterials, *Biomaterials*, 2019, **222**, 119451.
27 R. Mo and Z. Gu, Tumor microenvironment and intracellular signal-activated nanomaterials for anticancer drug delivery, *Mater. Today*, 2016, **19**, 274–283.
28 W. Xie, G. Zhang, Z. Guo, J. Lu, J. Ye, W. Xu, X. Gao, K. Yue, Y. Wei and L. Zhao, Ultra-Sensitive Iron-Doped Palladium Nanocrystals with Enhanced Hydroxyl Radical Generation for Chemo-/Chemodynamic Nanotherapy, *Adv. Funct. Mater.*, 2022, **32**, 2107518.
29 Z. Tang, Y. Liu, M. He and W. Bu, Chemodynamic Therapy: Tumour Microenvironment-Mediated Fenton and Fenton-like Reactions, *Angew. Chem., Int. Ed.*, 2019, **58**, 946–956.
30 X. Li, Q. Zhou, A. Japir, D. Dutta, N. Lu and Z. Ge, Protein-Delivering Nanocomplexes with Fenton Reaction-Triggered Cargo Release to Boost Cancer Immunotherapy, *ACS Nano*, 2022, **16**, 14982–14999.
31 S. Koo, O. K. Park, J. Kim, S. I. Han, T. Y. Yoo, N. Lee, Y. G. Kim, H. Kim, C. Lim, J. S. Bae, J. Yoo, D. Kim, S. H. Choi and T. Hyeon, Enhanced Chemodynamic Therapy by Cu-Fe Peroxide Nanoparticles: Tumor

Microenvironment-Mediated Synergistic Fenton Reaction, *ACS Nano*, 2022, **16**, 2535–2545.

32 J. M. Joseph, H. Destaillats, H.-M. Hung and M. R. Hoffmann, The Sonochemical Degradation of Azobenzene and Related Azo Dyes: Rate Enhancements via Fenton's Reactions, *J. Phys. Chem. A*, 2000, **104**, 301–307.

33 J. E. Kumar, T. Mulai, W. Kharmawphlang, R. N. Sharan and M. K. Sahoo, Decolourisation, mineralisation and detoxification of mixture of azo dyes using Fenton and Fenton-type advanced oxidation processes, *Chem. Pap.*, 2020, **74**, 3145–3159.

34 H. S. Sasmal, A. Halder, H. S. Kunjattu, K. Dey, A. Nadol, T. G. Ajithkumar, P. R. Bedadur and R. Banerjee, Covalent Self-Assembly in Two Dimensions: Connecting Covalent Organic Framework Nanospheres into Crystalline and Porous Thin Films, *J. Am. Chem. Soc.*, 2019, **141**, 20371–20379.

35 S. Sheng, F. Liu, M. Meng, C. Xu, H. Tian and X. Chen, Dual Reactive Oxygen Species Generator Independent of Light and Oxygen for Tumor Imaging and Catalytic Therapy, *CCS Chem.*, 2022, **4**, 2321–2332.

36 S. Chandra, T. Kundu, S. Kandambeth, R. Babarao, Y. Marathe, S. M. Kunjir and R. Banerjee, Phosphoric acid loaded azo (-N horizontal lineN-) based covalent organic framework for proton conduction, *J. Am. Chem. Soc.*, 2014, **136**, 6570–6573.